Ceramics International 47 (2021) 19073–19078

Contents lists available at ScienceDirect

Ceramics International

journal homepage: www.elsevier.com/locate/ceramint

# Synthesis of $ZnWO_4$ by the polymerizable complex method: Evidence of amorphous phase coexistence during the phase formation process

Magda S.S. Gondim [a], Eliezer C. Silva [b], Ananias L. dos Santos [b], Marcelo de Assis [c], José M. R. Mercury [a,1], Edson R. Leite [c,d], Içamira C. Nogueira [e,*]

[a] PPGEM, Federal Institute of Maranhão, 65030-005, São Luís, MA, Brazil
[b] PPGCEM, Federal University of Amazonas, 69077-000, Manaus, AM, Brazil
[c] Chemistry Department, Federal University of Sao Carlos, 13565-905, São Carlos, SP, Brazil
[d] Brazilian Nanotechnology National Laboratory (LNNano), CNPEM, 13083-100, Campinas, SP, Brazil
[e] Physics Department, Universidade Federal do Amazonas, 69077-000, Manaus, AM, Brazil

ARTICLE INFO

*Keywords:*
Calcination
Precursors: organic
Powders: chemical preparation
Amorphous
Phase transformations

ABSTRACT

In this paper, we report on a new path of $ZnWO_4$ phase formation, synthesized by the polymerizable complex (PC) method. At 550 °C, we obtained a single phase of the $ZnWO_4$ complex oxide. To explain the phase transformation processes, we propose a mechanism based on the coexistence of more than one amorphous phase after the pre-pyrolysis process. These amorphous metastable phases indicate a different phase formation path, which has not yet been described in the literature for multi-component oxides processed by the PC method. The formation path proposed here shows the relevance of the metastable phases in the reaction processes of complex oxides.

## 1. Introduction

In recent years, more in-depth studies on phase transformation kinetics, which take into account the stability of metastable phases, have promoted a better understanding of phase formation routes of multi-component oxides, leading to the development of more predictable synthesis routes [1–3]. Among the different synthetic routes to prepare complex multi-component oxides, the Pechini-type polymerizable complex (PC) method can be highlighted [4,5]. The PC method allows for very high stoichiometric control, leading to obtaining complex multi-component oxides, such as $BaTiO_3$ [4,6], $SrTiO_3$ [4,7], $KTiNbO_5$ [5], $SrBi_2Ta_2O_9$ [8], and others [4,5,9].

Briefly, the PC method adopts the metal complex formation from the reaction of a hydroxycarboxylic acid (mostly citric acid (CA)) with a soluble metal precursor. Under heating, the CA-complex undergoes an esterification reaction with polyhydroxy alcohol (ethylene glycol (EG)) to produce a polymeric resin throughout, ensuring homogeneous distribution and avoiding the segregation of different metallic ions immobilizing them in a rigid polyester network. Within this strategy, we ensure the initial cation ratio stoichiometry and the chemical homogeneity of the mixture at a molecular level leading to the crystallization of the desired inorganic phase without any spurious phases at low temperature [4,10]. Even when we identify an intermediate metastable compound, it has the cation ratio stoichiometry of the targeted compound. For instance, Leite et al. studied the synthesis of $PbTiO_3$ using the PC method and the authors reported the crystallization of a cubic $PbTiO_3$ phase, which evolves to the tetragonal $PbTiO_3$ phase with an increase in time and/or temperature [11,12]. On the other hand, when precipitation occurs during the polymerization step, homogeneity at a molecular level is lost and the phase formation process is controlled by a solid-state reaction. This situation must be avoided while synthesizing multi-component oxides via the PC method [13].

In recent years, we have observed that the scientific community has shown great interest in complex oxides of the wolframite tungstate oxide family [14,15]. Among these oxides, we can highlight $ZnWO_4$ as a poly-functional material with attractive photoluminescent properties, as well as potential candidates for photocatalytic applications, and humidity sensors [16–18]. During the synthesis of $ZnWO_4$ by the PC method, we noticed a different phase formation path from those reported so far in the literature. This path goes through the formation of

* Corresponding author.
*E-mail address:* isamiracosta@ufam.edu.br (I.C. Nogueira).
[1] in memoriam.

https://doi.org/10.1016/j.ceramint.2021.03.253
Received 13 October 2020; Received in revised form 12 March 2021; Accepted 24 March 2021
Available online 28 March 2021

more than one amorphous phase during the pre-pyrolysis step. In this article, we will describe this new crystallization path.

## 2. Material and methods

In this work, the $ZnWO_4$ was synthesized by the PC method, as follows. In this synthesis, zinc nitrate hexahydrate ($Zn(NO_3)_2.6H_2O$) (98%, Isofar), tungstic acid ($H_2WO_4$) (99%, Sigma-Aldrich), EG ($C_2H_6O_2$) (99%, Isofar), CA ($C_6H_8O_7$) (99.5%, Isofar) and ammonium hydroxide solution ($NH_4OH$) (28% $NH_3$ in $H_2O$, Isofar) were used as starting materials.

Initially, CA was dissolved in deionized water heated at 75 °C under constant stirring. Afterwards, $H_2WO_4$ was dissolved in deionized water using $NH_4OH$ and added to the CA solution. The formed tungstate citrate solution was stirred at 75 °C until a clear and homogeneous solution was obtained. Afterwards, $Zn(NO_3)_2.6H_2O$ was dissolved and added in a stoichiometric quantity to the citrate solution under agitation and at the same temperature. A CA/Metal molar ratio of 3:1 was used. After solution homogenization, EG was added to promote a polyesterification reaction. No visible precipitation was observed during the polymerization step. The citric acid/ethylene glycol ratio in mass was fixed at 60/40. The obtained transparent polymeric resin was then pre-pyrolyzed in a conventional furnace at 350 °C for 4 h. Finally, the obtained pre-pyrolyzed precursor was heat treated at 400, 450, 500 and 550 °C for 4 h under air atmosphere.

The phase evolution was followed by simultaneous thermal analysis (TG-DSC model STA 409 Netzsch), thermogravimetric analysis (TG) with differential scanning calorimetry (DSC), using a 10 °C/min heating rate with a synthetic airflow of 20 $cm^3$/min. The crystalline phases were identified by X-ray diffraction using a DMax/2500 PC diffractometer (Rigaku, Japan) with $CuK_\alpha$ radiation ($\lambda = 1.5406$ Å), at room temperature, in the 2θ ranging from 20 to 60° with a step size of 0.02°$min^{-1}$. A detailed analysis of the phases was performed by Rietveld refinement using the General Structure Analysis System (GSAS) software [19]. Diffrac-TOPAS (Bruker) software, using the relationship between peak areas, was performed to estimate the crystallized fraction. The Rietveld routines adopted a 2θ ranging from 10 to 110° with a step size of 0.02°$min^{-1}$, exposure time of 2s. The theoretical diffraction pattern was taken from the Inorganic Crystal Structure Database (ICSD) no. 84540 [20] and no. 50727 [21]. The refined parameters were the scale factor, background fitting with the Chebyschev polynomial of the first kind, shift lattice constants, profile half-width parameters, isotropic thermal parameters, lattice parameters, strain anisotropy factor, preferential orientation, and atomic functional positions. The phase formation and morphological evolution processes were also analyzed by Field Emission Scanning Electron Microscopy (FE-SEM FEI Inspec F-50 and FE-SEM Zeiss Supra) coupled with an Energy Dispersive X-Ray Spectroscopy (EDS). The FE-SEM analysis was performed at low (3 kV) and high (15 kV) voltages using a high-sensitive solid-state backscattered detector (vCD FEI detector), as well as an in-lens detector for secondary electron image analysis.

## 3. Results and discussion

### 3.1. Phase formation path

Fig. 1 shows the TG-DSC simultaneous thermal analysis results. In the TG curve, a total weight loss of 64% can be observed (Fig. 1a), suggesting that a significant amount of the organic precursor material is still present in the pre-pyrolyzed precursor. Four peaks related to the thermal decomposition of the residual organic material can be observed in the differential thermogravimetric (DTG) analysis (Fig. 1a, inset). The DSC curve of the pre-pyrolyzed precursor illustrated in Fig. 1b shows one endothermic peak at 75 °C and three exothermic peaks. It can be observed that the peaks reported in the DSC analysis match well with those reported in the DTG analysis (inset in Fig. 1a). Thus, we can attribute all these DSC peaks to the thermal decomposition of the residual organic material. The intense exothermic reaction observed, related to the thermal decomposition of the residual organic material, should cover the signal of peaks related to other exothermic events, explaining why we cannot identify peaks related to phase transformation, such as crystallization.

Since we were unable to follow the crystallization process of the $ZnWO_4$ precursor by TG-DSC, we used *"ex-situ"* XRD analysis to follow the $ZnWO_4$ phase evolution as a function of the temperature and the results are shown in Fig. 2. As can be seen, the pre-pyrolyzed precursor treated at 400 °C (Fig. 2a) showed a diffraction pattern characteristic of amorphous material, without the presence of any crystalline phase. At 450 °C (Fig. 2b), we observed the first diffraction peaks, which were indexed to the $WO_3$ crystalline phase (monoclinic structure, space group P21/n, Inorganic Crystal Structure Database (ICSD) nº 50727). This was the first phase to crystallize. However, we still observed a significant amount of the amorphous phase. Rising the temperature to 500 °C (Fig. 2c), we observed the coexistence of three phases, i.e. amorphous, $WO_3$, and $ZnWO_4$ (monoclinic structure, Inorganic Crystal Structure Database (ICSD) nº 84540). At 550 °C (Fig. 2d), all diffraction peaks were indexed to the $ZnWO_4$ crystalline phase, which was the only phase present. The sharp and well-defined diffraction peaks at 550 °C indicated a high degree of structural order, proving the effectiveness of the PC method used in this work to obtain single-phase crystalline $ZnWO_4$.

A detailed Rietveld refinement XRD analysis was performed in the samples heat treated at 500 °C and 550 °C (see Figure S1 in the support

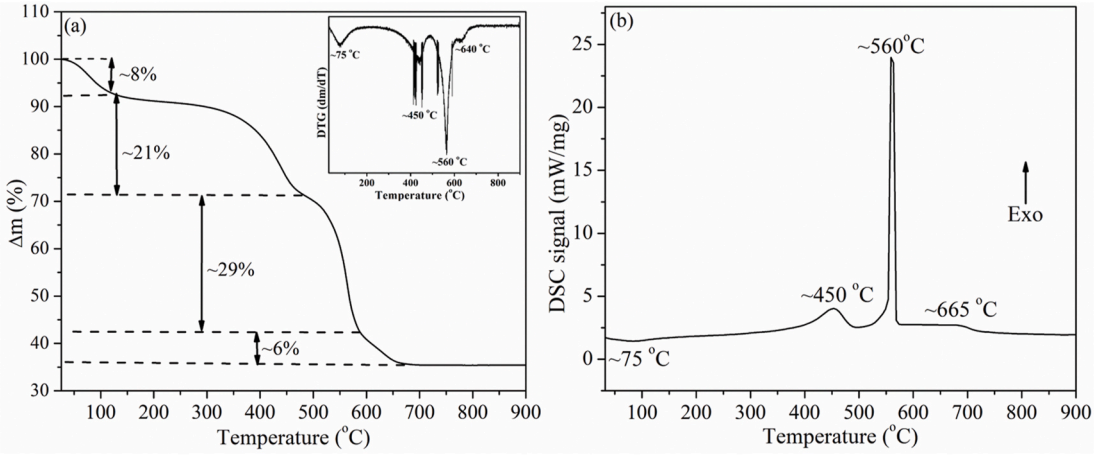


**Fig. 1.** TG-DSC simultaneous thermal of the pre-pyrolyzed precursor. a) TG and DTG (inset) analysis; b) DSC analysis.

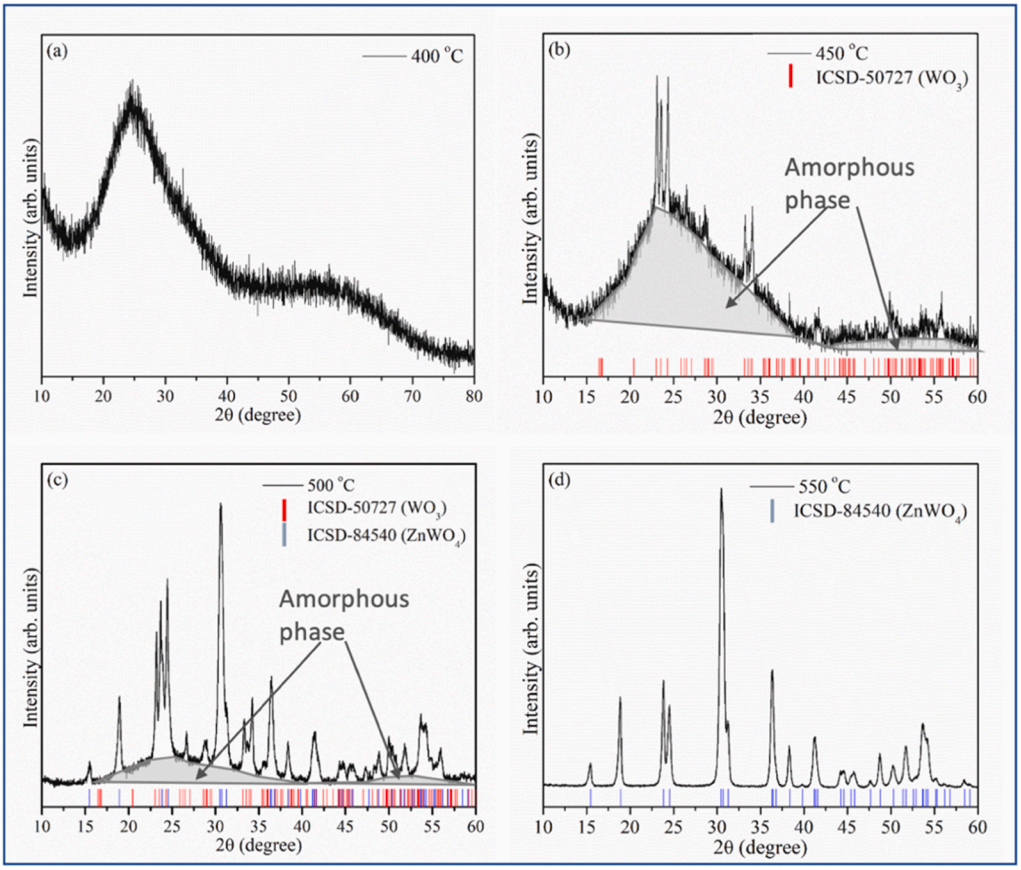


**Fig. 2.** XRD analysis of the pre-pyrolyzed materials treated at different temperatures, during 4 h. a) 400 °C; b) 450 °C; c) 500 °C; d) 550 °C.

information) using GSAS Software. This analysis confirmed the presence of the two crystalline phases at 500 °C, as previously reported in Fig. 2c, as well as the presence of a single phase ($ZnWO_4$) at 550 °C. At 500 °C, a semi-quantitative phase analysis (carried out by Diffract-TOPAS software) showed concentrations of 80.3% and 19.7% of crystalline and amorphous phases, respectively (see Figure S2 in the support information). Taking into account the crystalline phases only, a concentration of 27% and 73% of $WO_3$ and $ZnWO_4$ was identified, respectively. The

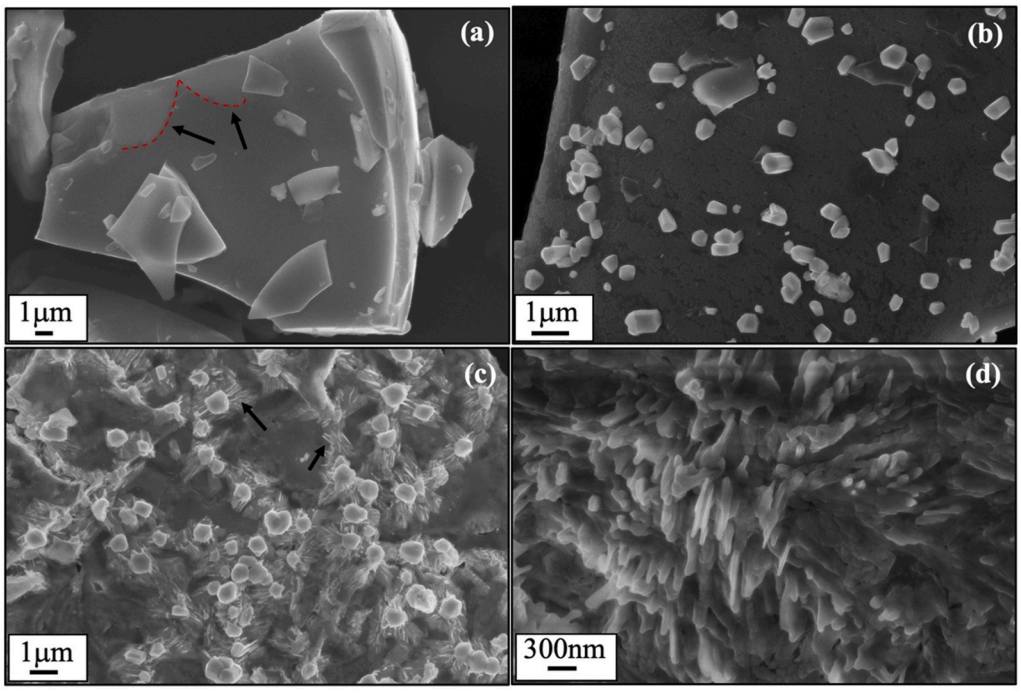


**Fig. 3.** –FE-SEM analysis, using SE image, of the pre-pyrolyzed materials treated at different temperatures, during 4 h. a) 400 °C; b)450 °C; c)500 °C; d) 550 °C.

structural crystallographic parameters and statistical indices of quality obtained from the Rietveld refinement are listed in Table S1 (see support information). The simulation performed by the TOPAS and GSAS showed very close values in agreement with the theoretical diffraction pattern used.

The phase evolution was also followed by FE-SEM using the secondary electron (SE) image, as shown in Fig. 3. As can be observed in Fig. 3a, the material treated at 400 °C shows a plate morphology, without the presence of grains. The absence of particulates is in agreement with the XRD data, which indicated the presence of an amorphous phase. In this sample, we also noticed the presence of regions with a different contrast and texture (indicated by the arrow). This different texture may indicate the presence of a second amorphous phase, which could not be identified by the XRD analysis. Increasing the temperature to 450 °C (Fig. 3b), we observed the appearance of well-faceted crystals with sub-micrometric dimensions originating from the amorphous matrix. The XRD data (Fig. 2b) indicates that they are $WO_3$ crystals. At 500 °C, we observed (Fig. 3c), a very complex structure, formed by the crystals of $WO_3$, a second phase with crystalline characteristics (indicated by arrows) and the presence of the amorphous phase. The second phase with crystalline features was identified by XRD as $ZnWO_4$ (Fig. 2c). Finally, at 550 °C (Fig. 3d), we observed a material with a granular texture, i.e. an agglomerate formed by primary elongated particles of irregular sizes, similar to the morphology previously observed for $ZnWO_4$ crystals formed at 500 °C. XRD analysis illustrated in Fig. 2d shows that at this temperature the granular material was in the $ZnWO_4$ phase.

To obtain more detailed information about the sample treated at 500 °C, we performed FE-SEM analysis using the vCD detector at low and high operation voltage, as well as EDS analysis. The results are shown in Fig. 4. Fig. 4a shows the SE image collected at 3 kV in the vCD detector, where the presence of faceted crystals of $WO_3$ and the presence of a crystalline phase (identified as $ZnWO_4$ by XRD) located near the $WO_3$ crystals can be observed, as well as spread by the amorphous matrix. Fig. 4b shows an image of BSE obtained at 15 kV, where the atomic number (Z) contract is clear. In this image, $WO_3$ (which has a higher Z) presents a bright contrast and the regions richer in Zn present a darker contrast. EDS spot analysis performed in regions # 1 and # 2 (see Fig. 4c) reinforce that the brighter crystals are $WO_3$ and that the crystals from region # 2 are richer in Zn, supporting the XRD analysis that indicates the presence of $ZnWO_4$. It is important to note that the spatial resolution of the EDS is around 1 μm, therefore signals from the regions adjacent to the one analyzed can also contribute to the X-ray fluorescence signal. Fig. 4d–e shows high-resolution SE images, where we see the presence of the well-faceted $WO_3$ crystals (see detail in the inset of Fig. 4d), $ZnWO_4$ crystals in contact with the $WO_3$ crystals, as well as $ZnWO_4$ crystals spread in the amorphous matrix without being in contact with the $WO_3$ crystals (See Fig. 4e).

### 3.2. General discussion

As reported before, after the pre-pyrolysis, the XRD and FE-SEM analyses show the following phase formation sequence, as a function of the calcination temperature.

$$\text{Amorphous} \rightarrow WO_3 + \text{Amorphous} \rightarrow WO_3 + \text{Amorphous} + ZnWO_4 \rightarrow ZnWO_4 \quad (1)$$

When we analyzed the sequence of phase transformations described in equation (1), we noticed the presence of amorphous phases in the different stages of the reaction path. The presence of different amorphous phases during the phase formation process is supported by the FE-SEM analysis, shown in Fig. 3a–b. Another relevant point is that at the end of the reaction process we have the formation of only the $ZnWO_4$ crystalline compound, without the presence of spurious phases,

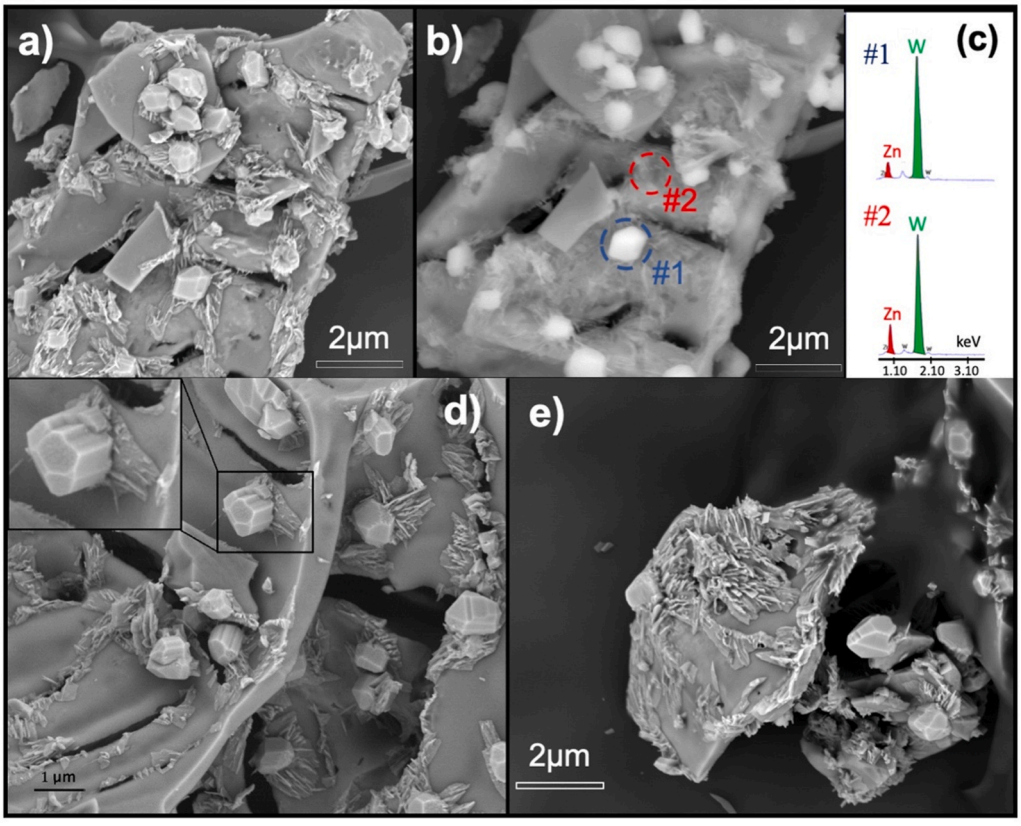


**Fig. 4.** FE-SEM analysis using the vCD detector at a) 3 kV (SE image); b) 15 kV (BSE image); c) EDS analysis of regions # 1 and #2; d-e) high resolution of the SE image. The inset shows details of the $WO_3$ crystal.

indicating that the stoichiometric ratio [Zn]/[W] = 1 is conserved.

We propose two hypotheses to explain the reaction path reported here. Hypothesis 1 takes into account the coexistence of several amorphous phases. After the pre-pyrolysis stage, three distinct amorphous phases are formed. One phase is rich in W (named as α), and the second phase is rich in Zn (α"). Finally, the third phase presents a stoichiometric ratio of metallic ions [Zn]/[W] = 1 (named as α'). These three phases coexist in the pre-pyrolyzed material, clearly showing a metastable equilibrium among them.

The sequence of phase formation of this hypothesis requires the coexistence of amorphous phases with different stability in relation to the crystallization process. In this hypothesis, the least stable amorphous phase is the α phase, followed by phase α'. The most stable amorphous phase is the Zn-rich phase (α").

The chemical reaction equations (2)–(4) summarize the chemical transformation proposed by hypothesis 1. Upon heating, the α phase crystallizes, giving rise to $WO_3$. By increasing the temperature once more, we notice that the $ZnWO_4$ formation took place in two different events, following different formation mechanisms. The first one occurs via the crystallization process from an amorphous phase (see equation (3); α' →$ZnWO_4$). The second mechanism is via the solid-state reaction between α" and $WO_3$ (see equation (4); $WO_3$ + α" → $ZnWO_4$'; where $ZnWO_4$' is the tungstate formed in a second event). It is interesting to note that we did not observe the formation of crystalline ZnO, reinforcing the hypothesis of solid-state reaction between the crystalline $WO_3$ and the amorphous α" phase to form the $ZnWO_4$ crystalline phase. The reaction between the crystalline $WO_3$ and the α" phase occurs via a solid-state mechanism, requiring the formation of a reaction interface between this phase and the crystalline $WO_3$ phases (reaction front), as well as a diffusional process to propagate the reaction front, resulting in the crystalline $ZnWO_4$.

$$\alpha + \alpha' + \alpha'' \rightarrow WO_3 + \alpha' + \alpha''\ 400\ ^\circ C < T < 450\ ^\circ C \quad (2)$$

$$WO_3 + \alpha' + \alpha'' \rightarrow WO_3 + \alpha'' + ZnWO_4\ 450\ ^\circ C < T < 500\ ^\circ C \quad (3)$$

$$WO_3 + \alpha'' + ZnWO_4 \rightarrow ZnWO_4 + ZnWO_4'\ T > 550\ ^\circ C \quad (4)$$

The second hypothesis takes into account the coexistence of two amorphous phases after the pre-pyrolysis step; one amorphous phase rich in W (α), and the second phase rich in Zn (α"). Upon heating, the α phase crystallizes, giving rise to $WO_3$ (see eq. (5)). By increasing the temperature, the reaction between crystalline $WO_3$ and the α" phase occurs, leading to the $ZnWO_4$ phase formation, via a solid-state reaction (see eq. (6)). The chemical reactions, equations (5) and (6), describe the chemical transformation proposed in hypothesis 2.

$$\alpha + \alpha'' \rightarrow WO_3 + \alpha''\ 400\ ^\circ C < T < 450\ ^\circ C \quad (5)$$

$$WO_3 + \alpha'' \rightarrow ZnWO_4\ T > 500\ ^\circ C \quad (6)$$

We notice now the $ZnWO_4$ formation took place in a single event and in a longer range of temperature (for T > 500 °C), following a solid-state reaction between α" and $WO_3$ (see eq. (6)). In both hypotheses, we consider the coexistence of more than one amorphous phase, showing a new alternative for a phase formation path in the PC method. However, the electron microscopy study (Figs. 3c and Fig. 4d–e) clearly shows the presence of the $ZnWO_4$ crystalline phase spread across the amorphous matrix. This detail is strong evidence against the formation of the $ZnWO_4$ phase in a single event by the solid-state reaction (as predicted by hypothesis 2), as this reaction requires the existence of a reaction front between the $WO_3$ and the α" phases during the whole reaction process. The existence of a third amorphous phase (with stoichiometry [Zn]/[W] = 1) and its direct crystallization into $ZnWO_4$ may explain the presence of this phase spread across the pre-pyrolyzed precursor. Thus, we believe that hypothesis 1 is the most plausible to describe the $ZnWO_4$ phase formation process prepared by the PC method.

Ryu et al. [22] reported the synthesis of the $ZnWO_4$ compound by the PC process; however, they observed a different phase formation path. They first reported the formation of $ZnWO_4$ and then the coexistence of $ZnWO_4$ and $WO_3$ phases, suggesting the existence of an amorphous phase rich in Zn. Moreover, they also reported the formation of the $ZnWO_4$ single phase as the final product, at 600 °C. The different routes of crystallization observed between our work and that reported by Ryu et al. [22] must be related to the different routes used to obtain the polymeric resin. As described in the materials and methods section, we prepared the polymeric resin adding a soluble metal precursor and CA in water, and then added EG. On the other hand, Ryu et al. [22] made the whole reaction by adding the soluble metal precursor and CA directly to the EG. This procedure must have generated a polymeric resin with a different chemical distribution of the cation mixture. Therefore, this different polymeric resin induced a different phase formation path.

## 4. Conclusions

In this work, we studied the formation of the $ZnWO_4$ phase via the PC method, as a function of the heat treatment temperature and observed a sequence of phase formation described in equation (1). At 550 °C, we obtained the $ZnWO_4$ complex oxide, without undesired phases. To explain the reaction and phase transformation processes, experimentally observed, we proposed two hypotheses, both based on the coexistence of more than one amorphous phase after the pre-pyrolysis process. The existence of these amorphous metastable phases indicates a different formation path, not yet described in detail in the literature for inorganic phases processed by the PC method. Finally, this study shows the relevance of the metastable phases in the reaction processes of complex oxides.

## Declaration of competing interest

The authors declare that they have no known competing financial interests or personal relationships that could have appeared to influence the work reported in this paper.

## Acknowledgments

This study was financed by the Coordenação de Aperfeiçoamento de Pessoal de Nível Superior - Brasil (CAPES) – Finance Code 001, Fundação de Amparo à Pesquisa do Estado do Amazonas, process number PPP-FAPEAM 062.01535/2018, Fundação de Amparo à Pesquisa do Estado de São Paulo (FAPESP), project number CEPID 2013/07296-2 and financed by the Conselho Nacional de Desenvolvimento Científico e Tecnológico (CNPq), process numbers, 312162/2019-7, 308263/2019-7 and Universal 439394/2018-0.

## Appendix A. Supplementary data

Supplementary data to this article can be found online at https://doi.org/10.1016/j.ceramint.2021.03.253.

## References

[1] A. Navrotsky, Nanoscale effects on thermodynamics and phase equilibria in oxide systems, ChemPhysChem 12 (2011) 2207–2215, https://doi.org/10.1002/cphc.201100129.

[2] M. Bianchini, J. Wang, R.J. Clément, B. Ouyang, P. Xiao, D. Kitchaev, T. Shi, Y. Zhang, Y. Wang, H. Kim, M. Zhang, J. Bai, F. Wang, W. Sun, G. Ceder, The interplay between thermodynamics and kinetics in the solid-state synthesis of layered oxides, Nat. Mater. 19 (10) (2020), https://doi.org/10.1038/s41563-020-0688-6, 0688–0693.

[3] B.-R. Chen, W. Sun, D.A. Kitchaev, J.S. Mangum, V. Thampy, L.M. Garten, D. S. Ginley, B.P. Gorman, K.H. Stone, G. Ceder, M.F. Toney, L.T. Chelhas, Understanding crystallization pathways leading to manganese oxide polymorph formation, Nat. Commun. 9 (2018) 2553, https://doi.org/10.1038/s41467-018-04917-y, 1-9.

[4] M. Kakihana, M. Yoshimura, Synthesis and characterization of complex multicomponent oxides prepared by polymeric complex method, Bull. Chem. Soc. Jpn. 72 (1999) 1427–1443, https://doi.org/10.1246/bcsj.72.1427.
[5] M. Kakihana, K. Domen, The synthesis of photocatalysts using the polymerizable complex method, MRS Bull. 25 (9) (2000) 27–31, https://doi.org/10.1557/mrs2000.176.
[6] M. Arima, M. Kakihana, Y. Nakamura, M. Yashima, M. Yoshimura, Polymerized complex route to barium titanate powders using barium-titanium mixed-metal citric acid complex, J. Am. Ceram. Soc. 79 (11) (1996) 2847–2856, https://doi.org/10.1111/j.1151-2916.1996.tb08718.x.
[7] E.R. Leite, C.M.G. Souza, E. Longo, J.A. Varela, Influence of polymerization on the synthesis of $SrTiO_3$: part I. Characterization of the polymeric precursors and their thermal decomposition, Ceram. Int. 21 (1995) 143–152, https://doi.org/10.1016/0272-8842(95)90903-V.
[8] S.M. Zanetti, E.R. Leite, E. Longo, J.A. Varela, Preparation and Characterization of $SrBi_2Nb_2O_9$ thin film made by polymeric precursors, J. Mater. Res. 13 (1998) 2932–2935, https://doi.org/10.1557/JMR.1998.0.
[9] E.R. Camargo, M. Kakihana, E. Longo, E.R. Leite, Pyrochlore-free $Pb(Mg_{1/3}Nb_{2/3})O_3$ prepared by a combination of the partial oxalate and polymerized complex methods, J. Alloys Compd. 314 (2001) 140–146, https://doi.org/10.1016/S0925-8388(00)01220–01222.
[10] M. Kakihana, T. Okubo, Low temperature synthesis of $LaAlO_3$ through in situ polymerization route utilizing citric acid and ethylene glycol, J, Alloys Compd 266 (1998) 129–133, https://doi.org/10.1016/S0925-8388(97)00445–3.
[11] E.R. Leite, E.C. Paris, E. Longo, J.A. Varela, Direct amorphous-to-cubic perovskite phase transformation for lead titanate, J. Am. Ceram. Soc. 83 (6) (2000) 1539–1541, https://doi.org/10.1111/j.1151-2916.2000.tb01427.x.
[12] E.R. Leite, E.C. Paris, E. Longo, F. Lanciotti Jr., C.E.M. Campos, P.S. Pizani, V. Mastellaro, Topotatic-like phase transformation of amorphous lead titanate to cubic lead titanate, J. Am. Ceram. Soc. https://doi.org/10.1111/j.1151-2916.2002.tb00429.x, 2002, 85, 9, 2166-2170.
[13] R. Polini, A. Pamio, E. Traversa, Effect of synthetic route on sintering behavior, phase purity and conductivity of Sr- and Mg-doped $LaGaO_3$ perovskites, J. Eur. Ceram. Soc 24 (2004) 1365–1370, https://doi.org/10.1016/S0955-2219(03)00592–2.
[14] Y. Jiang, B. Liu, Z. Zhai, X. Liu, B. Yang, L. Liu, X. Jiang, A general strategy toward the rational synthesis of metal tungstate nanostructures using plasma electrolytic oxidation method, Appl. Surf. Sci. https://doi.org/10.1016/j.apsusc.2015.08.080, 2015, 356, 273-281.
[15] X.A. López, A.F. Fuentes, M.M. Zaragoza, J.A.D. Guillén, J.S. Gutiérrez, A.L. Ortiz, V. Collins-Martínez, Synthesis, characterization and photocatalytic evaluation of MWO4 (M = Ni, Co, Cu and Mn) tungstates, Int. J. Hydrogen Energy 41 (48) (2016) 23312–23317, https://doi.org/10.1016/j.ijhydene.2016.10.117.
[16] D. Sivaganesha, S. Saravanakumara, V. Sivakumarb, R. Rajajeyaganthanc, M. Arunpandianc, J. Nandha Gopald, T.K. Thirumalaisamy, Surfactants-assisted synthesis of $ZnWO_4$ nanostructures: a view on photocatalysis, photoluminescence and electron density distribution analysis, Mater. Charact, 1-15, https://doi.org/10.1016/j.matchar.2019.110035, 2020, 159, 110035.
[17] M. Lia, Q. Menga, S. Li, F. Li, Q. Zhua, B.-N. Kim, J.-G. Li, Photoluminescent and photocatalytic $ZnWO_4$ nanorods via controlled hydrothermal reaction, Ceram. Int. 45 (8) (2019) 10746–10755, https://doi.org/10.1016/j.ceramint.2019.02.148.
[18] L. You, Y. Cao, Y.F. Sun, P. Sun, T. Zhang, Y. Du, G.Y. Lu, Humidity sensing properties of nanocrystalline $ZnWO_4$ with porous structures, Sensor. Actuator. B Chem. 161 (1) (2012) 799–804, https://doi.org/10.1016/j.snb.2011.11.035.
[19] A.C. Larson, R.B. Von Dreele, General structure analysis System (GSAS), Los Alamos National Laboratory Report LAUR 86-748 (1994). http://www.ccp14.ac.uk/solution/gsas/. (Accessed 15 April 2012).
[20] P.F. Schofield, K.S. Knight, S.A.T. Redfern, G. Cressey, Distortion characteristics across the structural phase transition in (Cu1-xZnx)WO4, Acta Crystallogr., B: Struct. Sci. Cryst 53 (1) (1997) 102–112, 10.1107/S0108768196010403.
[21] T. Vogt, P.M. Woodward, B.A. Hunter, The high-temperature phases of $WO_3$, J. Solid State Chem. 144 (1) (1999) 209–215, https://doi.org/10.1006/jssc.1999.8173.
[22] J.H. Ryu, C.S. Lim, K.H. Auh, Synthesis of $ZnWO_4$ nanocrystalline powders, by polymerized complex method, Mater. Lett. 57 (2003) 1550–1554, https://doi.org/10.1016/S0167-577X(02)01022-4.